Rare by Natural Selection: Tunable Disulfide-bonded Supramolecular Antimicrobials Peptides

Yizhaq Engelberg
Technion - Israel Institute of Technology
Peleg Ragonis-Bachar
Technion - Israel Institute of Technology
Meytal Landau (mlandau@technion.ac.il)
Technion - Israel Institute of Technology https://orcid.org/0000-0002-1743-3430

Article

Keywords: antimicrobial peptides, supramolecular fibrils, LL-37(17-29)

Posted Date: June 9th, 2021

DOI: https://doi.org/10.21203/rs.3.rs-578319/v1

Rare by Natural Selection: Tunable Disulfide-bonded Supramolecular Antimicrobials Peptides

Yizhaq Engelberg[1], Peleg Ragonis-Bachar[1], and Meytal Landau[1,2,*]

[1] Department of Biology, Technion-Israel Institute of Technology, Haifa 3200003, Israel

[2] European Molecular Biology Laboratory (EMBL), Hamburg 22607, Germany

*Correspondence to: mlandau@technion.ac.il

Short helical antimicrobial peptides forming inter-molecular disulfide bonds are selected against in nature, and were utilized here to design switchable antimicrobials via the formation of functional supramolecular fibrils. Specifically, using the available structural information on the stable fibril-forming human LL-$37_{17-29,}$ we designed cysteine mutations and demonstrated position-dependent controllable antibacterial activity, mediated by their disulfide-dependent self-assembly into ordered fibrils, which proved sensitive to reducing conditions. The crystal structure of the LL-37_{17-29} bearing a I24C substitution, located in a critical structural position, revealed disulfide-bonded dimers that further assembled into a fibrillar structure of densely packed helices. The native and mutant peptides both featured a fibril surface with zigzagged hydrophobic and positively charged belts, which likely underlie interactions with bacterial membranes. Yet, they differed in their helical packing arrangement, which corresponded with different levels of activity, with only the mutant being susceptible to reducing conditions. The presented findings promise to advance the design of novel antimicrobials resistant to harsh conditions for coating of surfaces susceptible to pathogens.

Introduction

Antimicrobial peptides (AMPs), secreted by numerous organisms, are critical for innate immunity, serving antibacterial, antiviral, anti-fungal, anticancer and immunomodulatory roles[1-3]. Host and microbes have evolved several mechanisms to regulate the activity of their own and foreign AMPs, which involve secreted proteases, virulence factors, and other substances[4-7]. For example, in-vivo cleavage of host AMPs can lead to truncated forms with a diverse array of activities and selectivity against microbial strains, alongside additional functions within the immune system[6,8-16]. Furthermore, secretion of reducing and oxidizing factors can regulate the activity of cysteine-containing AMPs that form disulfide bonds essential for their folding and activity[16-28]. For instance, pro-inflammatory processes involve oxidative stress through elevating reactive oxygen species (ROS) concentrations[23-25,29]. In parallel, some pathogens can promote and express reducing factors that diffuse the oxidative-dependent processes of inflammation and affect the activity of cysteine-rich AMPs[25,26,30]. Paradoxically, in the presence of elevated concentrations of a reduction agent, the antibiotic activity of the human β-defensin 3, which is a cysteine-rich AMP, decreased, while that of β-defensin 1 increased, indicating distinct structure-function relationships and physiological regulation of antimicrobial peptides via reductive pathways[28,29,31,32].

In contrast to the group of cysteine-rich AMPs, which are predominantly β-rich in their secondary structure, and usually form intramolecular disulfide bonds, AMPs with single cysteines can only form intermolecular disulfide contacts, yielding covalently bonded dimers. Since AMPs, especially helical amphipathic types, tend to self-assemble to enhance antimicrobial activity[33-40], such covalent dimers are expected to affect aggregation, with functional implications. We further expected that an intermolecular disulfide bond dictates the fibrillar morphology of short helical AMPs that assemble into functional ordered supramolecular structures, which can be reversed by reducing conditions. To test this hypothesis, we utilized the structural knowledge obtained for the active core peptide of the human AMP LL-37 (hLL-37_{17-29}), which forms highly stable supra-helical fibrils that interact

with bacterial cells[41]. We designed eight single-point cysteine mutations in different structural locations in hLL-37_{17-29} and analyzed their antibiotic activity against four bacterial strains, along with their sensitivity to reducing conditions. The observations were supported by cysteine substitutions in the amphibian uperin 3.5, another AMP that forms supramolecular structures, specifically of amyloid fibrils with a functional secondary structure switch between cross-α and cross-β configurations[42] . We further determined the atomic structure of a cysteine mutant at the center of the helical hydrophobic moment, the most deeply buried position in the assembly of hLL-37_{17-29}[41]. Overall, this work reinforces the importance of self-assembly in enabling the antibacterial activity of hLL-37_{17-29}, and demonstrates redox-switchable AMP activity, mediated by regulation of intermolecular disulfide bonds and their central role in the formation of supramolecular structures.

Results

Short amphipathic helical AMPs with an odd number of cysteines are rare

We sought to determine the abundance, among the thousands of AMPs included in the $CAMP_{R3}$ database[43], of short (<40 amino acids) amphipathic helical AMPs (sahAMP) which contain an odd number of cysteine residues, rendering them more likely to form dimers connected via intermolecular disulfide bonds. AMPs were defined helical according to a secondary structure prediction performed by the Jpred server[44] . AMPs were defined as amphipathic if the hydrophobic moment (μH) of the helical part of the sequence was above the average μH for all short helical AMPs. Despite the relatively high abundance of cysteine residues in AMPs, compared to proteins in general (Figure 1), the prevalence of sahAMPs with an odd number of cysteines was especially low (Supplementary Figure 1). Specifically, we found that among 662 sahAMPs, only 16 contained an odd number of cysteine residues (Supplementary Figure 1 and Supplementary Table 1). All but one of these 16 sequences had a single cysteine. In comparison, the prevalence of sahAMPs with an odd number of tyrosines, a residue which shows similar secondary structure propensities to cysteine[45], was significantly

higher (43 sequences), despite the lower abundance of tyrosines in short AMPs (Figure 1 & Supplementary Figure 1). The high number (153 sequences) of sahAMPs with an odd number of arginines, a residue which shows similar abundance in short AMPs to cysteine, again emphasizes the strong selection against sahAMPs with an odd number of cysteines.

Figure 1. Amino acid prevalence in AMPs and proteins in general

	Swiss-Prot	Swiss-Prot < 40aa	AMPs < 100aa	AMPs < 40aa
W	1.2	1.3	1.6	1.5
C	1.6	4.2	7.2	5.9
H	2.3	1.5	2.2	2.1
M	2.4	3.1	1.3	1.1
Y	3.1	2.7	2.6	1.9
Q	3.9	3.3	3.0	2.6
F	4.1	5.3	3.9	4.5
N	4.3	3.9	3.9	3.3
P	4.7	5.0	4.5	4.0
R	5.3	6.1	6.2	5.8
D	5.3	3.5	2.7	2.1
T	5.5	4.8	4.2	4
I	5.9	6.9	5.8	6.7
K	6.0	6.8	9.8	10.9
E	6.6	3.5	3.1	2.1
V	6.7	7.4	5.6	5.9
G	6.9	8.2	10.8	11.1
S	6.9	6.2	5.7	5.4
A	7.8	7.0	7.5	8.6
L	9.6	9.3	8.2	10.5

The figure outlines amino acid frequencies in four groups: proteins from the Swiss-Prot database[46] (n=563972), proteins shorter than 40 amino acids from the Swiss-Prot database (n=9526), AMPs shorter than 100 amino acids from the $CAMP_{R3}$ database[43] (n=2916), and AMPs shorter than 40 amino acids from the $CAMP_{R3}$ database[43] (n=2103). The amino acid frequencies are presented as percentage (%), indicating its relative abundance. The color code ranges from lowest to highest prevalence, colored in increasingly deep shades of blue to red, respectively.

The hLL-37_{17-29} I24C mutant forms supra-helical fibrils with inter-molecular disulfide bonds

In a recent characterization of the atomic details of stable supra-helical hLL-37_{17-29} fibrils[41], we report on fibrils composed of a basic unit of four-helix bundles with a hydrophobic core, with Ile24 located at the center of the bundle, completely buried within this assembly[41]. Substituting this position with alanine (I24A), which is less bulky and hydrophobic, or with various polar residues, fully abolished the ability of hLL-37_{17-29} to inhibit the growth of *M. luteus*, as well as

its ability to form ordered supramolecular structures[41] . We hypothesized that a substitution to cysteine will maintain inter-molecular associations via the formation of a stabilizing disulfide bond in the center of the hydrophobic face of the hLL-37_{17-29} amphipathic helix.

Solving the crystal structure of the hLL-37_{17-29} I24C mutant at 1.5Å resolution (PDB code 7NPQ, Supplementary Table 2), revealed a fibrillar structure of densely packed helices (Figures 2&3 and Supplementary Figure 2). The asymmetric unit contained two chains of amphipathic helices covalently connected via a disulfide bond between Cys24, with the hydrophobic sides facing each other (Supplementary Figure 3). The dimers were further assembled into a tightly packed structure, with a different fibrillar assembly compared to the native hLL-37_{17-29}, yet also displaying densely packed helices[41] (Supplementary Figure 3). While the four helix-bundles of hLL-37_{17-29} and the dimers of the I24C mutant showed a different orientation of helices, in both the hydrophobic face comprised a large portion of the inter-helical interface (Supplementary Figure 3 and Supplementary Table 3).

In hLL-37_{17-29} I24C, only a mean 17% of the solvent-accessible surface areas of individual helices, was buried within the dimer, yet 65% of the solvent-accessible surface area of chain A, and 78% of that of the chain B, was buried within the general assembly, indicating overall compact fibrillar packing. In comparison, in the fibrillar structure of the native hLL-37_{17-29}, on average, 67% of the solvent-accessible helix surface area was buried within the assembly[41] , showing similar compactness compared to the structure of hLL-37_{17-29} I24C (Supplementary Table 3). Both hLL-37_{17-29} and the I24C mutant structures displayed much tighter packing compared to the crystal structure of full-length LL-37, in which only 45% of the helix buried within the protein assembly was composed of associated dimers (for PDB ID 5NNT)[47].

Figure 2. Fibrillar atomic structure of the hLL-37$_{17-29}$ I24C mutant

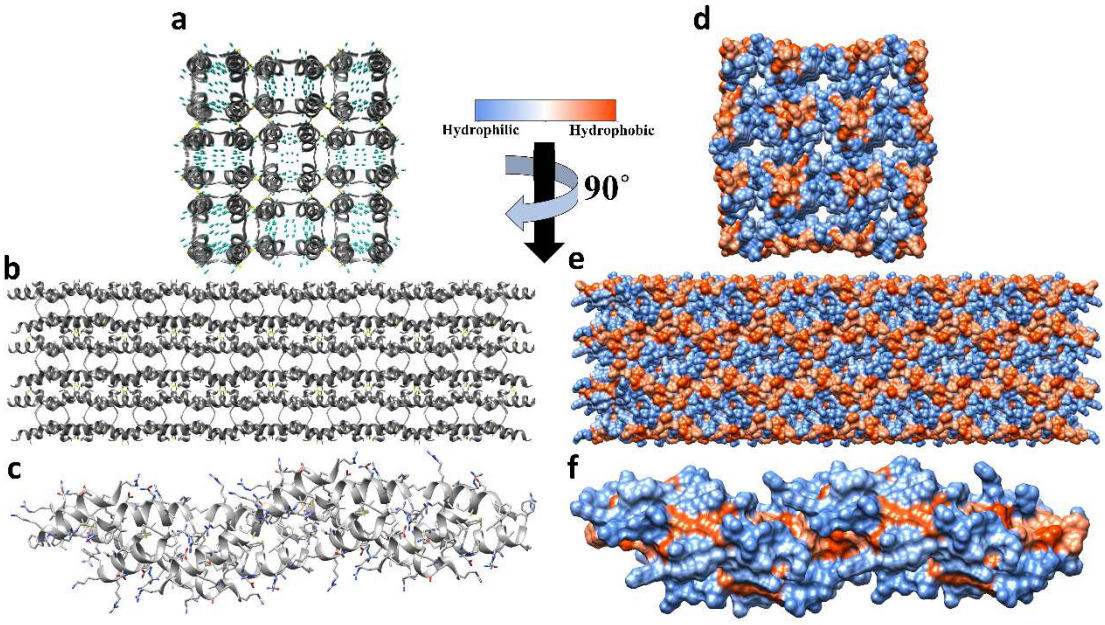

The crystal structure of the hLL-37$_{17-29}$ I24C mutant, determined at 1.5 Å resolution (PDB code 7NPQ, supplementary table 2), displays a self-assembled fibrillary structure of densely packed helices. (a-c) The hLL-37$_{17-29}$ I24C helices are presented as gray ribbons. Cysteine residues are shown as sticks and colored by atom type, with sulfur in yellow. In panel c, side chains are shown as sticks and colored by atom type, with nitrogen in blue and oxygen in red. (d-f) The same orientations as in panels a-c, respectively, displayed in a surface representation colored by hydrophobicity, according to the scale bar, demonstrating zigzagged belts of hydrophobic and polar interfaces. (a&d) Top view down the fibril axis. Water molecules are presented as cyan balls in panel a, emphasizing the alternating "dry" and hydrophobic cores, versus the "wet" and polar cores. (b&e) The orientation is rotated by 90˚ relative to panels a&d, for a view along the fibril axis. (c&f) An isolated helical assembly of an elongated protofibril encapsulating the hydrophobic core.

The four helix-bundles of the native hLL-37$_{17-29}$ further assembles via polar interactions and a small hydrophobic patch[41]. Similarly, in the I24C structure, covalent dimers further assembled via a network of interactions (Supplementary Figure 4), including putative salt bridges between Asp26 on chain A in one dimer and Lys18 on chain B of an adjacent dimer, and between Asp26 on chain B and Arg29 of chain A of an adjacent helix. In addition, the carboxyl group of the C terminus of chain A formed putative salt bridges with the side chain of Arg23 of chain A of another dimer and with the side chain of Arg29 from chain B of a third dimer. The carboxyl group of the C terminus of chain B formed putative salt bridges with the

side chain of Arg23 of chain B of a fourth dimer. Overall, each dimer was involved in 10 putative salt bridges with five surrounding dimers. The fibrillar assembly was further stabilized by Π-stacking and cation-Π interactions between two Phe17 residues from different dimers and two Arg23 residues from both chains of a third dimer (Figure 3). Moreover, an elongated hydrophobic core extended along the fibril. The top-view into the fibril axis depicts the hydrophobic core, tightly packed and completely deficient of water molecules (Figure 2 and Supplementary Figure 2). The side-view of the fibril depicts the helical assembly encapsulating the hydrophobic core into an elongated protofibril. The packing between these elongated protofibrils is mostly polar, mediated by water molecules and polar interactions (Figure 2 and Supplementary Figures 2&4).

Figure 3. Disulfide-bound helical dimers of the hLL-37$_{17-29}$ I24C mutant further assemble into a fibril via a network of cation-Π and hydrophobic interactions

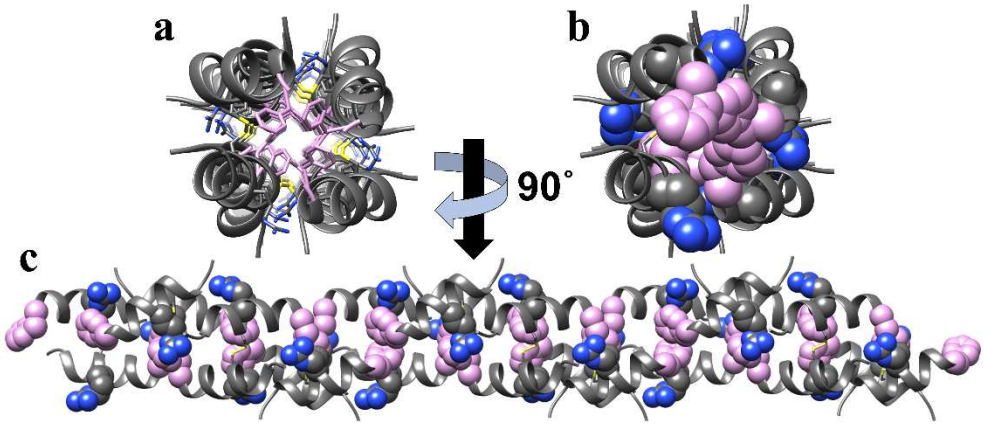

The hLL37(17-29) I24C protofibril encapsulating the hydrophobic core is shown in a grey ribbon representation. (a-b) A view down the fibril axis. (c) A side-view along the fibril axis of the protofibril, rotated 90˚ compared to panels a-b. Phe17 side chains are colored pink, and Arg23 and Cys24 side chains are colored by atom type (nitrogen in blue and sulfur in yellow). Phe17 and Arg23 are presented as sticks (a) or as space-filled atoms (b&c). Cys24 is presented as sticks in all panels. Close contacts between the aromatic Phe17 and the side chain of Arg23 suggests Π-stacking and cation-Π interactions that further stabilize the protofibril core.

The electrostatic potential map of the elongated protofibril showed a positively charged surface (Supplementary Figure 5), similar to the hLL-37$_{17-29}$ structure, which has arginine

residues lining the surface of the four-helix bundles[41]. Overall, despite the different general assembly, hLL-37_{17-29} and the I24C mutant both displayed a fibrillar structure with a surface composed of zigzagged hydrophobic and positively charged belts, which likely indicate interactions with and subsequent disruption of negatively charged lipid bilayers, such as bacterial membranes.

Formation and reduction of disulfide bonds in hLL-37_{17-29} cysteine mutants affect antibiotic activity and selectivity

The contribution of intermolecular disulfide bond formation to antibiotic activity and selectively was assessed using eight single-point cysteine mutations in different locations along the helical wheel of the amphipathic hLL-37_{17-29} (Supplementary Figure 6). Antibiotic activity against *Micrococcus luteus*, *Staphylococcus hominis*, *Escherichia coli* and *Pseudomonas fluorescens*, is shown as minimal inhibitory concentrations (MICs) of bacterial growth (Figure 4). While the native hLL-37_{17-29} and all mutants displayed similar MIC values against *M. luteus*, which lay with the range of 12-22 μM, they differed in their activity against other bacterial species (Figure 4 and Supplementary Figures 7-10).

For some of the active mutants, the addition of a reducing agent, dithiothreitol (DTT), abolished activity (Figure 4 and Supplementary Figures 7-10), indicating the functional significance of disulfide-mediated intermolecular assemblies. The sensitivity to DTT was the least pronounced in the activity of peptides against *M. luteus*, in which only hLL-37_{17-29} I24C lost activity with the addition of DTT (Supplementary Figure 7). The I24C mutant was not active against the other bacterial species, regardless of DTT, rendering it the least active mutant (Figure 4). DTT abolished activity of all active mutants against *S. hominis*, except for that bearing the K18C substitution, and that of all active mutants against *E. coli*, except of the F17C and Q22C mutants (Supplementary Figures 8-9). *P. fluorescens* was relatively resistant to all hLL-37_{17-29} peptides, which were either non-active or showed higher MICs compared to other bacteria strains (Supplementary Figure 10). However, in contrast to other bacterial species, *P. fluorescens* showed sensitivity to DTT itself (Supplementary Figure 11). The effect of DTT on the activity of the hLL-37_{17-29} peptide variants with high MIC values against *P. fluorescens*

thus could not be determined without considerable error resulting from the toxic effect of DTT alone. From what we could still determine, namely for the more active mutants F17A, V21C, and L28C, DTT abolished their activity against *P. fluorescens* (Figure 4).

For all bacterial species tested, the effect of DTT on antibiotic activity was mostly observed around the MIC concentrations of the peptides, while it was ineffective at supra-MIC concentrations (Supplementary Figures 7-10). This is likely due to the ability of these mutants to form active supramolecular or aggregated structures at high concentrations, independent of the disulfide bond.

Figure 4. Antibiotic activity and DTT sensitivity of hLL-37$_{17-29}$ with single-point cysteine mutants

	M. luteus		***S. hominis***		***E. coli***		***P. fluorescens***	
	MIC (μM)	DTT sensitivity	MIC (μM)	DTT sensitivity	MIC (μM)	DTT sensitivity	MIC (μM)	DTT sensitivity
hLL-37$_{17-29}$	25±2	-	39±1	-	47±3	-	136±4	-
F17C	22±2	-	64±6	+	63±5	+	164±5	+
K18C	16±3	-	50±8	-	100±7	+	>200	O
I20C	22±2	-	150±10	+	75±3	+	>200	O
V21C	17±3	-	43±7	+	30±0	+	113±5	+
Q22C	12±4	-	48±8	+	40±0	-	166±5	N/A
I24C	22±4	+	>200	o	>200	O	>200	O
F27C	13±3	-	28±5	+	37±3	+	151±3	N/A
L28C	20±0	-	37±3	+	43±3	+	75±3	+

Growth inhibition of four bacterial species by hLL-37$_{17-29}$ and hLL-37$_{17-29}$ with one of eight single-point cysteine mutants, indicated by MIC values, tested up to 200μM. The cells are colored from most to least active (lowest to higest MICs) colored blue to red, respectively. The ability of DTT, at x10 molar ratio compared to peptide concentration, to abolish activity, is indicated by (+) or (-), as detailed in supplementary Figures 7-10. In cases of non-bactericidal peptides, sensitivity to DTT was not relevant and the effect is marked with (o). Cases in which the DTT was too toxic for the bacteria at the indicated concentrations are marked by N/A. Mutant sensitivity to DTT was manually scaled and is indicated is the left column using a gray color scale, with light to dark shades indicate low to high DTT sensitivity, respectively. The MIC determination and DTT sensitivity experiments were performed at least four times each, on different days. Error values of MIC values indicate the standard error of all repeat measurements.

Reduction of disulfide bonds dissembled hLL-37_{17-29} I24C but not the Q22C mutant

The effect of DTT on self-assembly was evaluated by assessing the particle size distribution of the peptides using dynamic light scattering (DLS) (Supplementary Figure 12 and Supplementary Table 4). The particle size population of native hLL-37_{17-29}, with an average diameter of ~300 nm, indicating large assemblies, was not affected by the addition of DTT. In contrast, hLL-37_{17-29} I24C displayed a drastic DTT-dependent reduction in particle sizes, which had an average diameter of 1.3 nm, which roughly corresponds to a small oligomer of few subunits. Specifically, while untreated hLL-37_{17-29} I24C samples contained only ~34% small particles, and the remainder were large particles with an average size of ~340 nm, their abundance increased to ~100% on the addition of DTT. This indicates that self-assembly of I24C is very much dependent on disulfide bond formation, and can be reversed by a reducing agent. In contrast to the effect of DTT on I24C, it had no effect on the Q22C particle size distribution, which had an average diameter of ~360 nm, similar to the native hLL-37_{17-29}, suggesting that a disulfide bond is either not involved, or not critical for the formation of supramolecular species.

Self-assembly in the presence of *M. luteus* bacterial cells

The possible correlation between self-assembly of hLL-37_{17-29} structures, inter-molecular disulfide bonds and antibiotic activity was evaluated by electron microscopy, imaging the effect of the mutants on *M. luteus* cells. The active I24C mutant formed clustered structures on the membranes of *M. luteus*, while the addition of DTT led to amorphous aggregation around the bacterial membrane (Figure 5b&e), corresponding with its inhibitory effect on bactericidal activity (Figure 4). The F27C mutant, whose activity against *M. luteus* was not affected by the addition of DTT, formed dense aggregations on the bacterial membranes, while the addition of DTT resulted in the formation of defined fibril structures (Figure 5c&f). Overall, self-assembly into aggregated species or defined fibrils appeared to correlate with antibiotic activity, while disassembly to amorphous species (Figure 5) abolished this activity. Depending on the position of the cysteine, the inter-molecular disulfide bonds may play a role in

rearranging or supporting, but not necessarily in forming, the supra-helical assembly, as also suggested for the assembly of a transmembrane helix bundle[31].

Figure 5. Self-assembly of the hLL-$37_{17\text{-}29}$ I24C and F27C mutants around bacterial cells in the presence versus absence of a reducing agent

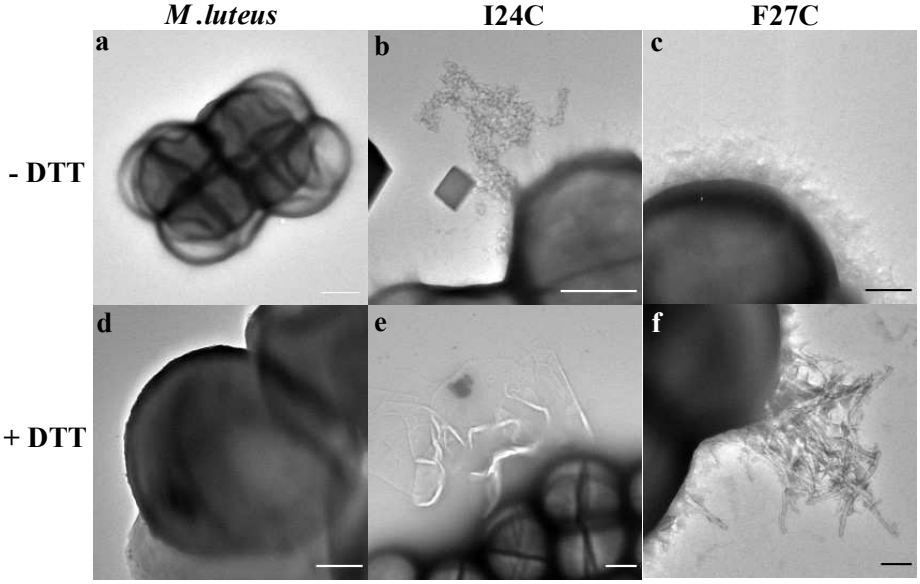

Electron micrographs of *M. luteus* incubated alone (a), with 1 mM DTT (d), or with the hLL-$37_{17\text{-}29}$ I24C (b-c) or hLL-$37_{17\text{-}29}$ F27C (c-f) mutants added at supra-MIC concentrations of 40 µM and 50 µM, respectively. The peptides and bacteria were incubated for 4 h without (b&c) or with (e&f) DTT at x12.5 or x17 molar ratio compared to the concentrations of I24C and F27C, respectively. Scale bars represent 500 nm (panels a-c&e) and 200 nm (panels d&f).

Reduction of disulfide bonds also affects antibiotic activity of the amphibian uperin 3.5 sahAMP

To assess the generality of DTT sensitivity of sahAMP cysteines mutants, we designed mutations in uperin 3.5, a sahAMP secreted on the skin of Australian toadlets. Uperin 3.5 was recently shown to form amyloid cross-α fibril structures of tightly mated helical sheets, formed via helices stacked perpendicular to the fibril axis[42]. The cross-α configuration was initially observed in the cytotoxic bacterial PSMα3[48], which shows similar sequence attributes to hLL-$37_{17\text{-}29}$, along with the shared ability to form fibrils composed of densely packed helices[41]. We designed uperin 3.5 with one of two cysteine mutations, I13C and S11C, located at the center

of the hydrophobic and polar faces of the helix, respectively. Both the native uperin 3.5, and its I13C and S11C mutants, were active against *M. luteus*, with MICs of 5-7 µM (Supplementary Table 5). While DTT had no effect on the activity of native uperin 3.5, it reduced that activity of both mutants (Figure 6 and Supplementary Table 5), with a greater impact on the I13C mutant (located on the hydrophobic face) as compared to the S11C mutant (located on the hydrophilic face). This is likely due to more efficient supramolecular fibrillar structure formation when the disulfide bond strengthens the hydrophobic intermolecular interfaces.

Figure 6. Cysteine mutants of the sahAMP uperin 3.5 show DTT-sensitive antibiotic activity

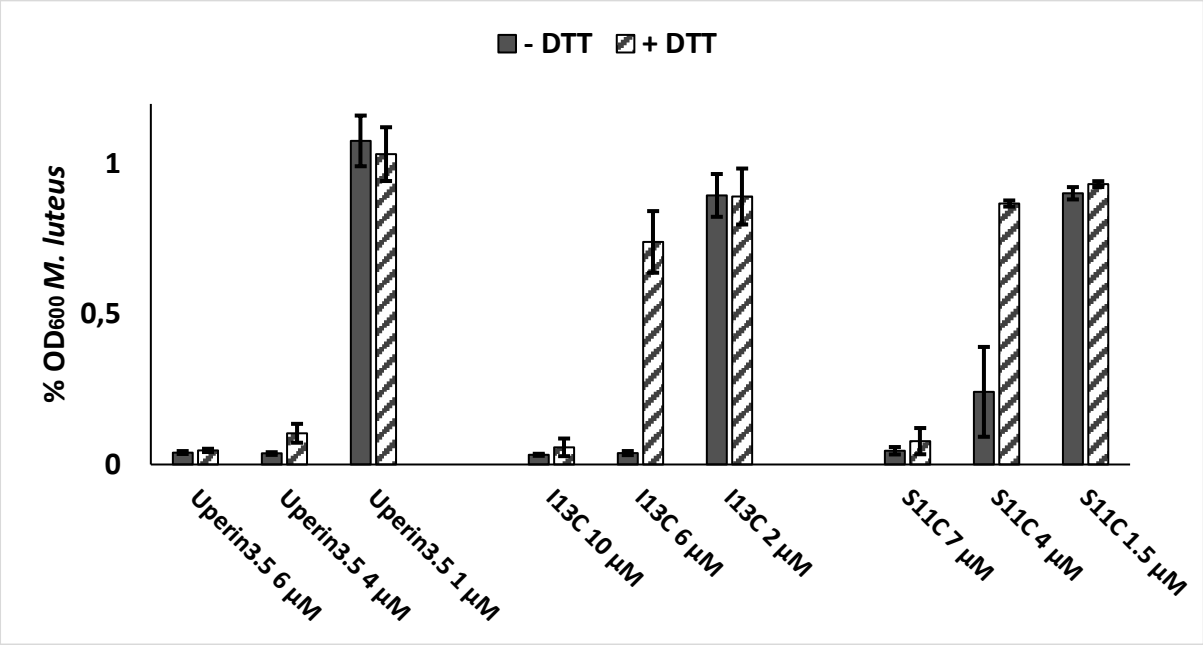

The effect of uperin 3.5 and of its I13C and S11C mutants on *M. luteus* bacterial growth was tested in the presence and absence of DTT. Bars show the ratio of *M. luteus* growth in the presence of the indicated peptides, compared to the bacteria growth without the peptide. DTT was added at x10 molar ratio compared to peptide concentration. The experiments were performed at least three times, on different days. Error bars represent the standard deviation of the mean of all biological repeats.

Discussion

AMPs are less likely to induce bacterial resistance compared to conventional small-molecule antibiotics, advocating their therapeutic value. Yet, their relatively low efficacy and lack of chemical stability have blunted their further development[49,50]. Here, we utilized structural information of the highly stable helical fibril of hLL-37_{17-29} and explored a means of chemically-controlled regulation of AMPs assembly into functional supramolecular structures. The tunability of disulfide bond-mediated supramolecular structures shown here for hLL-37_{17-29} was further demonstrated with amphibian uperin 3.5, which forms functional helical fibrils.

DTT abolished activity of all cysteine mutants of hLL-37_{17-29} against at least one bacterial species (Figure 4), indicating their disulfide-dependent specific bactericidal activity. Yet, the extent of the effect of DTT was dependent on the location of the cysteine substitution within the amphipathic helix, and was most prominent on the F17C, I20C, V21C and L28C mutants, which all bear substitution mutations on the hydrophobic face of the amphipathic helix (Supplementary Figure 6), where reduction of the disulfide bond destabilizes the formed supramolecular structure. Theoretically, a disulfide bond connecting the hydrophobic faces of sahAMPs would expose hydrophilic surfaces that would deter further amorphous aggregation, yet might promote ordered structures with specific inter-helical polar interactions, as was shown here by the atomic structure of the hLL-37_{17-29} I24C mutant.

Position Ile24 in hLL-37_{17-29} is located right at the center of the hydrophobic moment vector of the amphipathic helix (Supplementary Figure 6), and in the most buried core of the four-helix bundle of the hLL-37_{17-29} fibril[41] (Supplementary Table 3). In accordance with its critical structural location, substitutions of Ile24 to polar residues indeed abolished its antibiotic activity against *M. luteus*[41]. Even a milder substitution to alanine, which is more hydrophobic than cysteine, but still less hydrophobic than isoleucine[51] , abolished antibiotic activity against *M. luteus* and the formation of ordered fibrils of hLL-37_{17-29}[41] . It was therefore predicted that the activity of I24C, if any, will be dependent on the formation of disulfide bond-mediated assembly. The I24C mutant was not active against *S. hominis*, *E. coli* and *P. fluorescens.* It

remained active against *M. luteus*, but only under oxidizing conditions, which support the formation of a disulfide bond and assembly of supramolecular fibrils, as shown by the crystal structure (Figure 2). Reducing conditions indeed dissembled the ordered assembly of the I24C mutant, as demonstrated by the marked shift in particle size distribution towards small particles (Supplementary Figure 12 and Supplementary Table 4), and as visualized in Figure 5. The results further support the important role of self-assembly in hLL-37_{17-29} antibiotic activity[41].

DTT was least effective in altering the activity of the mutants bearing K18C and Q22C substitutions, which are located on the polar face of the helix (Figure 4 and Supplementary Figure 6). Theoretically, a disulfide bond connecting the polar face of the helix could hinder the formation of ordered fibrillar structures featuring a hydrophobic core. Therefore, one conjecture is that the K18C and Q22C mutants are active, to the same extent, as monomers, covalent dimers, or as amorphous aggregate. Yet a more plausible hypothesize is that these mutants self-assemble regardless of the formation of a disulfide bond via an extensive fibrillar hydrophobic core featuring a more extensive surface area buried along with a network of interactions, as shown for hLL-37_{17-29}[41] and its I24C mutant (Figures 2-3 and Supplementary Figures 2-4), compared to an isolated covalent dimer. In accordance with this hypothesis, while DTT had a significant effect on I24C activity, it had no effect on Q22C particle size distribution, which remained primarily composed of large particles (Supplementary Figure 12 and Supplementary Table 4).

Both crystal structures of hLL-37_{17-29} and its I24C mutant, although different, were associated with fibrillary structures, with a surface composed of zigzagged hydrophobic and positively charged belts, which likely disrupt bacterial membranes comprised of negatively charged lipid bilayers. DTT had different effects on peptide antibiotic activity, depending on the tested mutant and bacterial species, which might be indicative of diverse mechanisms of hLL-37_{17-29} mutant action against different bacteria. Moreover, the bacterial membranes and cell walls might differentially affect aggregation and fibril morphology, thereby altering toxicity level. Bi-directional effects between membrane lipids and fibril-forming toxins have been

previously suggested for the bacterial PSMα3 cytotoxin and the amphibian uperin 3.5 AMP which form helical cross-α amyloid fibrils[42,52,53].

To conclude, we demonstrated the feasibility of designing switchable antimicrobials that can be deactivated under reducing conditions, but remain active under oxidative conditions, such as in areas of inflammation[23-25]. Their dependence on oxidizing conditions can also be used to target activity of AMPs to act on cancerous cells[54]. It is possible that the observed selection against sahAMPs with an odd number of cysteine residues is due to the microorganisms' ability to express reducing factors[25-27]. Since AMP self-assembly can often bear functional relevance and enhance antimicrobial activity[33], another explanation to this negative selection could be that the intermolecular disulfide bonds lead to a reduction in the number of conformational states, and to reduced entropy, similarly to disulfide-mediated protein folding[55-60], thereby hindering peptide aggregation. The demonstrated control over AMP activity is enabled via regulation of its self-assembly into functional supramolecular structures, which can be used as scaffolds for a wide range of bio and nanotechnology, regenerative medicine and bioengineering applications[61], with the invaluable advantage of an inherent antibacterial activity. Our findings can specifically advance the design of novel antimicrobials with stability under harsh conditions, for coating of medical devices, food packages, water pipes and other surfaces susceptible to aggressive and resistant pathogens.

Methods

Peptides and reagents

hLL-37_{17-29} and uperin 3.5 (UniProt IDs P49913 and P82042, respectively) and their cysteine mutants were purchased from GL Biochem (Shanghai) Ltd. as lyophilized peptides, at >98% purity. Ultra-pure double distilled water (UPddw) and DTT were purchased from Biological Industries.

Bacterial strains and culture media

Micrococcus luteus (*M. luteus*, an environmental isolate) was a kind gift from Prof. Charles Greenblatt from the Hebrew University of Jerusalem, Israel. An inoculum was grown in Luria-Bertani medium (LB), at 30 °C, 220 rpm shaking, 16 h[42]. *Staphylococcus hominis* (subsp. *Hominis Kloos and Schleifer S. hominis*) was purchased from ATCC (ATCC® 27844™). An inoculum was grown in brain-heart infusion medium (BHI), at 37 °C, 220 rpm shaking, 16 h[41]. *Pseudomonas fluorescens* (*P. fluorescens*) was a kind gift from Prof. Roi Kishoni from the Technion, Israel. An inoculum was grown in LB, at 28 °C, with 220 rpm shaking, for 16 h[62,63]. *Escherichia coli*, subsp. *k3 3106* (*E. coli*) was a kind gift from Prof. Ehud Gazit from Tel Aviv University, Israel. An inoculum was grown in LB, at 37 °C, with 220 rpm shaking, for 16 h.

Dynamic light scattering (DLS)

The particles size distribution of hLL-37_{17-29} and its cysteine mutants, Q22C and I24C, with or without DTT, was compared using DLS. Lyophilized peptides were dissolved in UPddw to a concentration of 1 mM. DTT powder was freshly dissolved in UPddw to a concentration of 1M and was added to relevant peptides samples to a final concentration of 10mM. After a short vortex, the samples were incubated for 24 h, at 25 °C. Samples (20-30 µl) were then mounted using 1.0x1.0 mm disposable cuvette capillaries with a thickness of 200 µm (Malvern, ZSU0003), which were then sealed with clay. Capillaries were placed within low-volume disposable sizing cell Kitholder (Malvern, ZSU1002). Light scattering readings were collected using ZetaSizer Ultra (Ultra ZS; Malvern). The hydrodynamic radii (Rh) were determined using a back-scattered light at a fixed angle of 90°. A 633 nm wavelength He-Ne laser was used.

The cell holder was maintained at 25°C for the measurement. Scattering data were collected from at least three different measurements with at least five sequential scans for each measurement. The mean of the volume intensities was sub-categorized into three cumulative subpopulations (S.P) of sizes: 0.3-30 nm, 30-3000 nm and above 3000 nm (>3000 nm), to yield a cumulative volume of particles within the sample. The average size of each subcategory was determined by summing the score of the mean average volume intensities their correlative sizes within each range, as described elsewhere[34]. Error (E) was calculated by dividing the standard deviation at the square of the measurements number. Error bars indicate the cumulative error for each subpopulation and were calculated by squaring the sum of the squares of the error values in the subpopulation range.

Transmission electron microscopy (TEM)

To image the peptides in the presence of bacterial cells, *M. luteus* was grown for 24 h in LB, approximately 1.5×10^9 bacteria cells were washed three times by pelleting the bacteria suspension via centrifuging at 2000xg and replace the supernatant with 10 mM potassium phosphate buffer, pH = 7.4. Lyophilized peptides (hLL-$37_{17\text{-}29}$ I24C and F27C) were dissolved in the same buffer and added to the bacterial pellets, which were re-suspended to a final peptide concentration of 40–50 μM (as detailed in the relevant figures). DTT was freshly dissolved in UPddw to a stock solution of 1 M, which was further dissolved in the same buffer as the peptides to a concentration of 100 mM. DTT was applied to relevant peptides in x10 molar ratio excess relative to the peptide (specific concentrations are indicated in the relevant figures). Samples were then incubated at 30 °C, with 220 rpm shaking, for 2 h. TEM grid preparation and visualization were performed as follows: samples (4–5 μl) were applied directly onto glow-discharged (easiGlow; Pelco, Clovis, CA, USA, 15 mA current; negative charge; 25 s time) 400 mesh copper grids, with a grid hole size of 42 μm, stabilized with Formvar/carbon (Ted Pella, Inc.), and allowed to adhere for 45 s. Samples were than stained with 1% uranyl acetate solution (Electron Microscopy Science, 22400-1) for 30 s before being blotted with Whatman filter paper. Specimens were examined with a FEI Tecnai T12 G2

electron microscope, at an accelerating voltage of 120 kV, or a FEI Tecnai G2 T20 electron microscope, at an accelerating voltage of 200 kV.

Determination of minimal inhibitory concentrations (MIC)

M. luteus and *S. hominis* inocula were diluted to OD_{600} = 0.1. hLL-37_{17-29}, uperin 3.5 and cysteine mutants were dissolved in phosphate buffered saline (PBS) buffer into peptides stocks solutions. Peptides stocks solutions were then diluted in the bacteria medium. Control and blank samples contained everything but peptides or everything but bacteria, respectively. Experiments were performed in a sterile 96-well plate, with a final reaction volume of 100 µl. Bacterial growth (OD_{600}) was measured by a plate reader (FLUOstar omega or CLARIOstar, BMG LABTECH), during a 24 h incubation, at different temperatures (as described previously), with 220 rpm shaking. Blanks were subtracted and the ratio of the test samples versus their respective controls (everything but the peptide) were calculated. MIC values were defined as the minimal concentration of the peptide which yielded less than 20% of the OD_{600} ratios. All experiments were performed in triplicates and were averaged. The entire experiment was repeated at least three times on different days, and the mean was calculated from the averaged triplicates of all biological repeats. Error bars represent standard errors of the mean. For the DTT sensitivity experiments, DTT was freshly dissolved in UPddw to a stock with a concentration of 1 M, and diluted in PBS to working stocks of 200-300 mM. Stocks of peptides were initially dissolved in PBS and then DTT was added to a final concentration of x10 molar ratio compared to the peptide concentration (the specific concentrations are indicated in the relevant figures). Samples with DTT were compared to their relevant controls which contained everything but the peptides (and the same DTT concentrations). All experiments including controls and blanks, were tested in triplicates on at least three different days. Measurements were averaged. Appropriate blanks were subtracted, and the mean values were plotted against peptide concentration. Standard errors of the mean of OD_{600} readings are presented as error bars.

Crystallization conditions

I24C lyophilized peptide and DTT were both dissolved in UPddw to 10 mM (~17 mg/ml) and 100 mM, respectively. DTT was added to the peptide solution to a final concentration of 0.1 mM. Samples were vortexed and centrifuged (14,000 rpm, 4˚C, 10 min). Crystals of I24C with DTT were grown, at 20°C, from a reservoir solution containing 2.8 M sodium acetate trihydrate, pH 7.0. (Hampton Research, HR2-134 (Index HT), well B12), using the hanging-drop vapor diffusion technique. Crystals were flash-frozen in liquid nitrogen before X-ray data collection.

Structure determination and refinement

X-ray diffractions of I24C were collected at the EMBL micro-focused beam at the high brilliance 3rd Generation Synchrotron Radiation Source at DESY: PETRA III, Hamburg, Germany. The wavelength of data collection was 0.976Å. Data indexing, integration, and scaling were performed using XDS and XSCALE[64]. Phases were obtained by molecular replacement using Phaser[65]. Molecular replacement of I24C phases was performed using the atomic structure of $gLL37_{17\text{-}29}$ coordinates (PDB 6S6N) as a search model. Crystallographic refinements were performed with Refmac5 [66]. Model building was also performed using Coot[67] and illustrated with Chimera[68]. The structure of I24C was determined at 1.5 Å. There were two peptide chains in the asymmetric unit and 16 water molecules.No residues were detected in the disallowed region at the Ramachandran plot. Crystallographic statistics are presented in Supplementary Table 2.

Calculations of structural properties

The electrostatic potential map and hydrophobicity coloring presented in the figures were generated using Chimera[68]. The values of the hydrophobicity scale were according to Kyte and Doolittle[69]. The electrostatic potential was calculated using APBS-PDB2PQR[70]. Helix amphipathicity, and chemical and physical properties of sequences (Supplementary Figure 6) were calculated with HeliQuest[71]. The helical wheels were also generated by HeliQuest[71].

Solvent-accessible surface area calculations

Solvent-accessible surface areas (SASAs) were calculated using AREAIMOL, with a probe radius of 1.4Å[72,73], via the CCP4 package[66]. The solvent-accessible buried surface area of

each chain in the asymmetric unit was calculated as the area difference between the isolated chain and the chain within the fibril assembly, and is presented as the percentage of the total SASA of the chain. The SASA per residue within different isolated helical assemblies is presented in Supplementary Table 3.

Statistical analysis of amino-acid frequencies

Databases and protein groups analyzed

To calculate amino acid frequency in different protein groups, we used the Swiss-Prot database of curated proteins[46], and the ($CAMP_{R3}$) database[43] for a collection of anti-microbial peptides. All 20 amino acid frequencies were calculated in four different protein groups: proteins from the Swiss-Prot database[46] (n=563972 protein sequences (PG1)), proteins shorter than 40 amino acids from the Swiss-Prot database (n=9526 sequences (PG2)), AMPs shorter than 100 amino acids from the $CAMP_{R3}$ database[43] (n=2916 sequences (PG3)), and AMPs shorter than 40 amino acids from the $CAMP_{R3}$ database[43] (n=2103 sequences (PG4)). For each group, the frequency of each amino acid was calculated as follows:

$$frequency\ of\ amino\ acid\ X\ in\ PG\# = \frac{\sum_{p \in PG\#} number\ of\ amino\ acid\ X\ in\ p}{\sum_{p \in PG\#} length\ of\ p}$$

where PG# denotes the four different protein groups.

Secondary structure prediction and amphipathicity

The Jpred webserver[44] was used to predict secondary structures of each peptide in the databases. Jpred relies on the A Neural Network Protein Secondary Structure Prediction Method (JNet algorithm), one of the most accurate methods for secondary structure prediction[44]. To adapt the data to Jpred input requirements, amidation of Ctr or Ntr were removed (if existed) and peptides smaller than 20 amino acids were duplicated $\left\lfloor \frac{20}{peptide\ length} \right\rfloor$ times to obtain a minimum length of 20 amino acids. We defined the secondary structure as helical using three threshold values: (1) minimal number of residues predicted as helix is eight, or the residues predicted as helix encompass at least 80% of the sequence length (2) Minimal gap of four residues between segments predicted as helix and (3) Minimal Jpred predicted score of the helix is at least two, on average, over the predicted residues encompassing the

helix (this is considered a low threshold, over a range of probability scores going up to nine). Thus, we were permissive in defining helical sequences. The hydrophobic moment (μH) was calculated as $\frac{1}{N}\sqrt{[\sum_{n-1}^{N} H_n \sin(n\delta)]^2 + [\sum_{n-1}^{N} H_n(\cos(n\delta))]^2}$, where N is the sequence length, H_n is the hydrophobicity of the n[th] amino acid in the sequence according to its octanol\water partition[74] and $n\delta$ is the angle separating side chains along the backbone, with $\delta = 100°$ for an α-helix[75]. The μH threshold was determined as the mean μH calculated for all AMPs shorter than 40 amino acids that were predicted as helical, and helical sequences were defined as amphipathic in case the calculated μH was higher than the μH threshold.

Specific amino acid frequency calculations in sahAMPs

The number of sequences containing an odd number of cysteines was counted among AMPs shorter than 40 amino acids from the $CAMP_{R3}$ database[43], among short AMPs predicted as helical, and among those also defined as amphipathic. The numbers are presented in Supplementary Figure 1. As controls, the numbers of sequences from the same groups having an odd number of tyrosines, due to its similar helical propensity, according to the Cho-Fasman table[76] and of arginines, due to its similar frequency in sahAMPs as cysteine, were counted. To graphically present the number of AMPs containing an odd number of cysteine, tyrosine, or arginine (residue 'X'), normalized to their frequencies in AMPs shorter than 40 amino acids from the $CAMP_{R3}$ database[43], including 2103 sequences (PG4), we used :

$$\frac{Number\ of\ AMPs\ containing\ an\ odd\ number\ of\ \ residue\ 'X'}{'X'\ frequency\ in\ AMPs\ shorter\ than\ 40\ residues \cdot Number\ of\ AMPs\ horter\ than\ 40\ residues}$$

Acknowledgments

We would like to thank Eilon Barnea for critical comments and Leehen Mashiah for technical support. We acknowledge technical support provided by Yael Pazy-Benhar and Dikla Hiya at the Technion Center for Structural Biology (TCSB). We acknowledge guidance and support from Yaron Kauffmann from the MIKA Electron Microscopy Center of the Department of Material Science & Engineering at the Technion, and from Na'ama Koifman from the Russell Berrie Electron Microscopy Center of Soft Matter at the Technion, Israel. This research was supported by the Israel Science Foundation (grant no. 2111/20), Israel Ministry of Science, Technology & Space (grant no. 78567), U.S.-Israel Binational Science Foundation (BSF) (grant no. 2017280), BioStruct-X, funded by FP7, and the iNEXT consortium of Instruct-ERIC. The synchrotron MX data collection experiments were performed at beamline P14, operated by EMBL Hamburg at the PETRA III storage ring (DESY, Hamburg, Germany). We are grateful to the teams at EMBL Hamburg for their assistance.

References

1 Jenssen, H., Hamill, P. & Hancock, R. E. Peptide antimicrobial agents. *Clinical microbiology reviews* **19**, 491-511 (2006).

2 Shai, Y. From innate immunity to de-novo designed antimicrobial peptides. *Curr Pharm Des* **8**, 715-725, doi:10.2174/1381612023395367 (2002).

3 Mader, J. S. & Hoskin, D. W. Cationic antimicrobial peptides as novel cytotoxic agents for cancer treatment. *Expert opinion on investigational drugs* **15**, 933-946 (2006).

4 Lai, Y. *et al.* The human anionic antimicrobial peptide dermcidin induces proteolytic defence mechanisms in staphylococci. *Molecular microbiology* **63**, 497-506 (2007).

5 Gonzalez, D. J. *et al.* Novel phenol-soluble modulin derivatives in community-associated methicillin-resistant Staphylococcus aureus identified through imaging mass spectrometry. *Journal of Biological Chemistry* **287**, 13889-13898 (2012).

6 Wang, G. *et al.* Design of Antimicrobial Peptides: Progress Made with Human Cathelicidin LL-37. *Adv Exp Med Biol* **1117**, 215-240, doi:10.1007/978-981-13-3588-4_12 (2019).

7 Fialho, A. M., Stevens, F. J., Gupta, T. K. D. & Chakrabarty, A. M. Beyond hostق│ôpathogen interactions: microbial defense strategy in the host environment. *Current opinion in biotechnology* **18**, 279-286 (2007).

8 Epand, R. F., Wang, G., Berno, B. & Epand, R. M. Lipid segregation explains selective toxicity of a series of fragments derived from the human cathelicidin LL-37. *Antimicrobial agents and chemotherapy* **53**, 3705-3714 (2009).

9 Schmidtchen, A., Frick, I. M., Andersson, E., Tapper, H. & Bjorck, L. Proteinases of common pathogenic bacteria degrade and inactivate the antibacterial peptide LL-37. *Mol Microbiol* **46**, 157-168, doi:10.1046/j.1365-2958.2002.03146.x (2002).

10 Chen, Z. *et al.* Design and antimicrobial activities of LL-37 derivatives inhibiting the formation of Streptococcus mutans biofilm. *Chemical biology & drug design* (2019).

11 Wang, G., Mishra, B., Epand, R. F. & Epand, R. M. High-quality 3D structures shine light on antibacterial, anti-biofilm and antiviral activities of human cathelicidin LL-37 and its fragments. *Biochim Biophys Acta* **1838**, 2160-2172, doi:10.1016/j.bbamem.2014.01.016 (2014).

12 Johansson, J., Gudmundsson, G. H., Rottenberg, M. E., Berndt, K. D. & Agerberth, B. Conformation-dependent antibacterial activity of the naturally occurring human peptide LL-37. *J Biol Chem* **273**, 3718-3724, doi:10.1074/jbc.273.6.3718 (1998).

13 Deplanche, M. *et al.* Phenol-soluble modulin alpha induces G2/M phase transition delay in eukaryotic HeLa cells. *Faseb j* **29**, 1950-1959, doi:10.1096/fj.14-260513 (2015).

14 Joo, H. S., Cheung, G. Y. & Otto, M. Antimicrobial activity of community-associated methicillin-resistant Staphylococcus aureus is caused by phenol-soluble modulin derivatives. *J Biol Chem* **286**, 8933-8940, doi:10.1074/jbc.M111.221382 (2011).

15 Thwaite, J. E., Hibbs, S., Titball, R. W. & Atkins, T. P. Proteolytic degradation of human antimicrobial peptide LL-37 by Bacillus anthracis may contribute to virulence. *Antimicrobial agents and chemotherapy* **50**, 2316-2322 (2006).

16 Lee, J. U. *et al.* Solution structures and biological functions of the antimicrobial peptide, arenicin-1, and its linear derivative. *Peptide Science: Original Research on Biomolecules* **88**, 208-216 (2007).

17 Dimarcq, J. L., Bulet, P., Hetru, C. & Hoffmann, J. Cysteine-rich antimicrobial peptides in invertebrates. *Biopolymers* **47**, 465-477, doi:10.1002/(SICI)1097-0282(1998)47:6<465::AID-BIP5>3.0.CO;2-# (1998).

18 Boman, H. G. Peptide antibiotics and their role in innate immunity. *Annu Rev Immunol* **13**, 61-92, doi:10.1146/annurev.iy.13.040195.000425 (1995).

19 Gerdol, M., De Moro, G., Manfrin, C., Venier, P. & Pallavicini, A. Big defensins and mytimacins, new AMP families of the Mediterranean mussel Mytilus galloprovincialis. *Developmental & Comparative Immunology* **36**, 390-399 (2012).

20 Harris, P. W. *et al.* Plant antimicrobial peptides snakin1‖ | ق and snakin2‖ | ق: chemical synthesis and insights into the disulfide connectivity. *Chemistryق | ôA European Journal* **20**, 5102-5110 (2014).
21 Lehrer, R. I. & Ganz, T. Endogenous vertebrate antibiotics. Defensins, protegrins, and other cysteine-rich antimicrobial peptides. *Ann N Y Acad Sci* **797**, 228-239, doi:10.1111/j.1749-6632.1996.tb52963.x (1996).
22 Park, C. H., Valore, E. V., Waring, A. J. & Ganz, T. Hepcidin, a urinary antimicrobial peptide synthesized in the liver. *J Biol Chem* **276**, 7806-7810, doi:10.1074/jbc.M008922200 (2001).
23 Scott, M. G., Davidson, D. J., Gold, M. R., Bowdish, D. & Hancock, R. E. The human antimicrobial peptide LL-37 is a multifunctional modulator of innate immune responses. *The journal of immunology* **169**, 3883-3891 (2002).
24 Fang, F. C. Antimicrobial actions of reactive oxygen species. *mBio* **2**, doi:10.1128/mBio.00141-11 (2011).
25 Reniere, M. L. Reduce, induce, thrive: bacterial redox sensing during pathogenesis. *Journal of bacteriology* **200** (2018).
26 Mu, K., Wang, D. & Kitts, D. D. Molecular mechanisms that define redox balance function in pathogen-host interactions—is there a role for dietary bioactive polyphenols? *International Journal of Molecular Sciences* **20**, 6222 (2019).
27 Paiva, C. N. & Bozza, M. T. Are reactive oxygen species always detrimental to pathogens? *Antioxidants & redox signaling* **20**, 1000-1037 (2014).
28 Schroeder, B. O. *et al.* Reduction of disulphide bonds unmasks potent antimicrobial activity of human beta-defensin 1. *Nature* **469**, 419-423, doi:10.1038/nature09674 (2011).
29 Brzoza, P. *et al.* Redox Active Antimicrobial Peptides in Controlling Growth of Microorganisms at Body Barriers. *Antioxidants-Basel* **10**, doi:ARTN 446

10.3390/antiox10030446 (2021).
30 Wehkamp, J. *et al.* Reduced Paneth cell alpha-defensins in ileal Crohn's disease. *Proc Natl Acad Sci U S A* **102**, 18129-18134, doi:10.1073/pnas.0505256102 (2005).
31 Karim, C. B. *et al.* Role of cysteine residues in structural stability and function of a transmembrane helix bundle. *Journal of Biological Chemistry* **276**, 38814-38819, doi:DOI 10.1074/jbc.M104006200 (2001).
32 Bladon, C. M., Bladon, P. & Parkinson, J. A. Delta-toxin and analogues as peptide models for protein ion channels. *Biochemical Society transactions* **20**, 862-864 (1992).
33 Malekkhaiat Häffner, S. & Malmsten, M. Influence of self-assembly on the performance of antimicrobial peptides. *Curr Opin Colloid In* **38**, 56-79, doi:https://doi.org/10.1016/j.cocis.2018.09.002 (2018).
34 Engelberg, Y. & Landau, M. The Human LL-37(17-29) antimicrobial peptide reveals a functional supramolecular structure. *Nat Commun* **11**, 3894, doi:10.1038/s41467-020-17736-x (2020).
35 Tian, X., Sun, F., Zhou, X. R., Luo, S. Z. & Chen, L. Role of peptide self-assembly in antimicrobial peptides. *J Pept Sci* **21**, 530-539, doi:10.1002/psc.2788 (2015).
36 Haffner, S. M. & Malmsten, M. Influence of self-assembly on the performance of antimicrobial peptides. *Curr Opin Colloid In* **38**, 56-79, doi:10.1016/j.cocis.2018.09.002 (2018).
37 Lombardi, L. *et al.* Enhancing the Potency of Antimicrobial Peptides through Molecular Engineering and Self-Assembly. *Biomacromolecules* **20**, 1362-1374, doi:10.1021/acs.biomac.8b01740 (2019).
38 Lee, E. Y. *et al.* Helical antimicrobial peptides assemble into protofibril scaffolds that present ordered dsDNA to TLR9. *Nature Communications* **10**, doi:ARTN 1012 10.1038/s41467-019-08868-w (2019).

39 Leithold, L. H. *et al.* Pharmacokinetic Properties of a Novel D-Peptide Developed to be Therapeutically Active Against Toxic beta-Amyloid Oligomers. *Pharmaceutical research* **33**, 328-336, doi:10.1007/s11095-015-1791-2 (2016).

40 Wei, G. *et al.* Self-assembling peptide and protein amyloids: from structure to tailored function in nanotechnology. *Chemical Society Reviews* **46**, 4661-4708, doi:10.1039/C6CS00542J (2017).

41 Engelberg, Y. & Landau, M. The Human LL-37(17-29) antimicrobial peptide reveals a functional supramolecular structure. *Nature Communications* **11**, 3894, doi:10.1038/s41467-020-17736-x (2020).

42 Salinas, N. *et al.* The amphibian antimicrobial peptide uperin 3.5 is a cross-α/cross-β chameleon functional amyloid. *Proc Natl Acad Sci U S A* **118** (2021).

43 Waghu, F. H., Barai, R. S., Gurung, P. & Idicula-Thomas, S. CAMPR3: a database on sequences, structures and signatures of antimicrobial peptides. *Nucleic Acids Res* **44**, D1094-1097 (2016).

44 Drozdetskiy, A., Cole, C., Procter, J. & Barton, G. J. JPred4: a protein secondary structure prediction server. *Nucleic Acids Res* **43**, W389-394, doi:10.1093/nar/gkv332 (2015).

45 Kumar, T. A. CFSSP: Chou and Fasman secondary structure prediction server. *Wide Spectrum* **1**, 15-19 (2013).

46 Consortium, U. Update on activities at the Universal Protein Resource (UniProt) in 2013. *Nucleic Acids Res* **41**, D43-47, doi:10.1093/nar/gks1068 (2013).

47 Sancho-Vaello, E. *et al.* Structural remodeling and oligomerization of human cathelicidin on membranes suggest fibril-like structures as active species. *Sci Rep* **7**, 15371, doi:10.1038/s41598-017-14206-1 (2017).

48 Tayeb-Fligelman, E. *et al.* The cytotoxic Staphylococcus aureus PSMalpha3 reveals a cross-alpha amyloid-like fibril. *Science* **355**, 831-833, doi:10.1126/science.aaf4901 (2017).

49 Fox, J. L. Antimicrobial peptides stage a comeback. *Nature biotechnology* **31**, 379-382, doi:10.1038/nbt.2572 (2013).

50 Lei, J. *et al.* The antimicrobial peptides and their potential clinical applications. *Am J Transl Res* **11**, 3919-3931 (2019).

51 Diederichs, K. & Karplus, P. A. Improved R-factors for diffraction data analysis in macromolecular crystallography. *Nature structural biology* **4**, 269-275 (1997).

52 Tayeb-Fligelman, E., Salinas, N., Tabachnikov, O. & Landau, M. Staphylococcus aureus PSMalpha3 Cross-alpha Fibril Polymorphism and Determinants of Cytotoxicity. *Structure* **28**, 301-313.e306, doi:10.1016/j.str.2019.12.006 (2020).

53 Martin, L. L. *et al.* Amyloid aggregation and membrane activity of the antimicrobial peptide uperin 3.5. *Peptide Science* **110**, e24052, doi:10.1002/pep2.24052 (2018).

54 Shai, Y. Mode of action of membrane active antimicrobial peptides. *Biopolymers* **66**, 236-248, doi:10.1002/bip.10260 (2002).

55 Murphy, K. P. & Freire, E. Thermodynamics of structural stability and cooperative folding behavior in proteins. *Adv Protein Chem* **43**, 313-361, doi:10.1016/s0065-3233(08)60556-2 (1992).

56 Jensen, K. S., Hansen, R. E. & Winther, J. R. Kinetic and thermodynamic aspects of cellular thiol-disulfide redox regulation. *Antioxid Redox Signal* **11**, 1047-1058, doi:10.1089/ARS.2008.2297 (2009).

57 Peng, L., Qian, H. & Hong, L. Thermodynamics of Markov processes with nonextensive entropy and free energy. *Phys Rev E* **101**, 022114, doi:10.1103/PhysRevE.101.022114 (2020).

58 Brady, G. P. & Sharp, K. A. Entropy in protein folding and in protein-protein interactions. *Curr Opin Struct Biol* **7**, 215-221, doi:10.1016/s0959-440x(97)80028-0 (1997).

59 Betz, S. F. Disulfide bonds and the stability of globular proteins. *Protein Sci* **2**, 1551-1558, doi:10.1002/pro.5560021002 (1993).

60 Harrison, P. M. & Sternberg, M. J. Analysis and classification of disulphide connectivity in proteins. The entropic effect of cross-linkage. *J Mol Biol* **244**, 448-463, doi:10.1006/jmbi.1994.1742 (1994).
61 Hughes, S. A. *et al.* Ambidextrous helical nanotubes from self-assembly of designed helical hairpin motifs. *Proc Natl Acad Sci U S A* **116**, 14456-14464, doi:10.1073/pnas.1903910116 (2019).
62 Donnarumma, G. *et al.* Effect of temperature on the shift of Pseudomonas fluorescens from an environmental microorganism to a potential human pathogen. *Int J Immunopathol Pharmacol* **23**, 227-234, doi:10.1177/039463201002300120 (2010).
63 Rainey, P. B. Adaptation of Pseudomonas fluorescens to the plant rhizosphere. *Environ Microbiol* **1**, 243-257, doi:10.1046/j.1462-2920.1999.00040.x (1999).
64 Kabsch, W. XDS. *Acta Crystallogr D Biol Crystallogr* **66**, 125-132, doi:10.1107/s0907444909047337 (2010).
65 McCoy, A. J. *et al.* Phaser crystallographic software. *Journal of Applied Crystallography* **40**, 658-674, doi:doi:10.1107/S0021889807021206 (2007).
66 Winn, M. D. *et al.* Overview of the CCP4 suite and current developments. *Acta Crystallogr D Biol Crystallogr* **67**, 235-242, doi:10.1107/s0907444910045749 (2011).
67 Emsley, P. & Cowtan, K. Coot: model-building tools for molecular graphics. *Acta Crystallogr. D Biol. Crystallogr.* **60**, 2126-2132 (2004).
68 Pettersen, E. F. *et al.* UCSF Chimera--a visualization system for exploratory research and analysis. *J Comput Chem* **25**, 1605-1612, doi:10.1002/jcc.20084 (2004).
69 Kyte, J. & Doolittle, R. F. A simple method for displaying the hydropathic character of a protein. *J Mol Biol* **157**, 105-132, doi:10.1016/0022-2836(82)90515-0 (1982).
70 Jurrus, E. *et al.* Improvements to the APBS biomolecular solvation software suite. *Protein Science* **27**, 112-128, doi:10.1002/pro.3280 (2018).
71 Gautier, R., Douguet, D., Antonny, B. & Drin, G. HELIQUEST: a web server to screen sequences with specific alpha-helical properties. *Bioinformatics* **24**, 2101-2102, doi:10.1093/bioinformatics/btn392 (2008).
72 Saff, E. B. & Kuijlaars, A. B. Distributing many points on a sphere. *The mathematical intelligencer* **19**, 5-11 (1997).
73 Lee, B. & Richards, F. M. The interpretation of protein structures: estimation of static accessibility. *J Mol Biol* **55**, 379-400 (1971).
74 Fauchere, J. & Pliska, V. Hydrophobic parameters II of amino acid side-chains from the partitioning of N-acetyl-amino acid amides. *Eur. J. Med. Chem.* **18** (1983).
75 Eisenberg, D., Weiss, R. M. & Terwilliger, T. C. The helical hydrophobic moment: a measure of the amphiphilicity of a helix. *Nature* **299**, 371-374, doi:10.1038/299371a0 (1982).
76 Chou, P. & Fasman, G. D. Amino acid sequence. *Adv. Enzymol. Relat. Areas Molec. Biol* **47**, 45-55 (2009).

Supplementary Files

This is a list of supplementary files associated with this preprint. Click to download.

- D1292113255valreportfullP1.pdf
- SIEngerbergFK13Cys2021.7.pdf